

# A discrete model for laser driven etching and microstructuring of metallic surfaces

Alejandro Mora\* and Maria Haase†

*Institut für Höchstleistungsrechnen (IHR), University of Stuttgart, 70569 Stuttgart, Germany*

Thomas Rabbow‡ and Peter Jörg Plath§

*Institut für Angewandte und Physikalische Chemie, Chemische Synergetik,*

*University of Bremen, Bibliotheksstraße NW2, 28359 Bremen, Germany*

(Dated: May 23, 2019)

We present a unidimensional discrete solid-on-solid (SOS) model evolving in time using a kinetic Monte Carlo method to simulate micro-structuring of kerfs on metallic surfaces by means of laser-induced jet-chemical etching (LJE). The precise control of the passivation layer achieved by this technique is responsible for the high resolution of the structures. However, within a certain range of experimental parameters, the microstructuring of kerfs on stainless steel surfaces with a solution of  $H_3PO_4$  shows periodic ripples which are considered to originate from an intrinsic dynamics. The model mimics a few of the various physical and chemical processes involved and within certain parameter ranges reproduces some morphological aspects of the structures, in particular ripple regimes. We analyze the range of values of laser beam power for the appearance of ripples in both experimental and simulated kerfs. The discrete model is an extension of one that has been used previously in the context of ion sputtering and is related to a noisy version of the Kuramoto-Sivashinsky equation used extensively in the field of pattern formation.

PACS numbers: 61.82.Bg, 81.65.Cf, 05.10.Ln, 47.54.+r

## I. INTRODUCTION

Since the eighties, laser induced wet chemical etching in silicon, ceramics, and metals has been an intensively used micro-structuring technique [1]. Controlling the quality of the final structures is the main issue from the experimental and theoretical point of view. In a variation of the experimental technique developed by Metev, Stephen and collaborators (see [2],[3] and [4]) and currently implemented by Rabbow et al. (see [5]), a focussed laser beam enhanced by a coaxial jet of etchant induces an etching reaction producing holes and kerfs on metallic samples within a micrometer scale.

This technique is called *laser-induced jet-chemical etching* (LJE) and has been successful in fabricating super-elastic micro-grippers of nickel-titanium alloy. However, within a certain range of parameters, in the microstructuring of kerfs on stainless steel surfaces with a solution of  $H_3PO_4$ , unwanted periodic ripples appear. In this article, it is considered that these ripples are intrinsically generated and belong to a wide universality class of pattern formation phenomena that emerge for example, in ripple structures formed by wind over a sand bed, ion sputtering of various surfaces [6],[7] and abrasive water-jet cutting [8].

In the context of ion sputtering, Cuerno and collabora-

tors proposed a stochastic 1D discrete solid-on-solid (SOS) model based on the competition between erosion and diffusion processes in which ripples appear at early stages of the evolution [9]. We have extended and adapted this model for the LJE case taking into account a moving gaussian-distributed laser beam which leads to a localized heating and etching of the metallic sample. The motivation to use such a phenomenological model is originated in the limited knowledge of the interaction of diverse processes occurring in a wide range of scales. The dynamics of the laser light absorption, heat, chemical reactions, hydrodynamics and transport phenomena is too complex to be fully modelled. While this *extended model* is quite simple, it nevertheless captures essential physical effects of the process, such as the unstable temperature driven etching and the stabilizing mechanism of surface diffusion. In addition, since the model is evolved in time using a kinetic Monte Carlo method, fluctuations and rough surfaces are produced naturally.

This article is organized as it follows. In section II we present the basics of the experimental setup and describe qualitatively some of the relevant microscopic processes occurring during etching. The appearance of a ripple regime in a series of kerfs structured with increasing laser power is analyzed in section III. There a hypothesis about the intrinsic nature of the ripples is proposed. In section IV we describe and justify the extension of the Cuerno model, analyzing the scaling properties and ripple regimes for uniform erosion. The application of the extended model to simulate the LJE is presented in the section V. Varying the simulated laser power, a ripple regime is obtained and compared with the experimental one. In the conclusions we summarize achievements and

\*Electronic address: ica2am@csv.ica.uni-stuttgart.de

†Electronic address: ica2mh@csv.ica.uni-stuttgart.de

‡Electronic address: rabbow@uni-bremen.de

§Electronic address: plath@uni-bremen.de

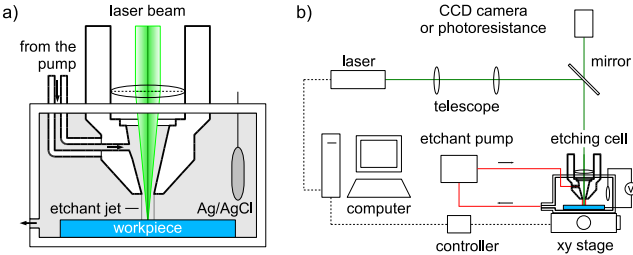


FIG. 1: Schematic diagram of the experimental setup. (a) The etching cell. A focussed laser induces an etching reaction enhanced by a coaxial running jet of the etchant. (b) The whole experimental setup. The reaction can be observed with a CCD-camera and the intensity of the reflected light is measured with a photo-resistance. Due to the laser induced etching the workpiece changes its state locally from passive to active. Changes of the potential are detected with an Ag/AgCl reference electrode.

shortcomings of the model and suggest future improvements.

## II. THE LJE TECHNIQUE

### A. The experimental setup

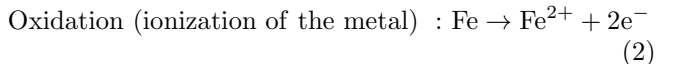
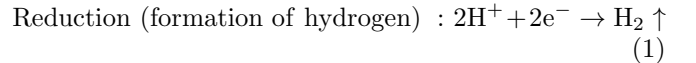
A schematic diagram of the etching cell is shown in figure 1(a). In this implementation of the technique, foils of stainless steel (Fe/Cr18/Ni10) and titanium are immersed horizontally in a solution of etchant based on 5M H<sub>3</sub>PO<sub>4</sub>. The microstructuring of the samples is achieved by an argon ion cw-laser beam at 514nm embedded coaxially in a jet of etchant liquid which is directed perpendicularly to the surface. The laser beam is focused by an optical system which creates a spot size smaller than 10 $\mu$ m. The laser induced etching leads to dissolution of the metal and formation of hydrogen. Simultaneously, changes of the state of the electrode from passive to active produce an electrochemical potential and its temporal evolution  $E(t)$  can be measured against an Ag/AgCl reference electrode which is immersed in the etching reservoir.

The etching cell is mounted on a computer-controlled mobile basis which allows to move the sample in  $xy$  plane with respect to the laser beam with different feed velocities (see figure 1(b)). The experimental setup is automated allowing to structure holes or kerfs varying the most relevant external parameters : laser power, etchant jet velocity, feed velocity and etchant concentration. Details of the process can be observed with a CCD camera located above the etching cell in the same axis of the laser beam. Alternatively, by means of a photo-resistance located in the same position, measurements of the intensity of the reflected light can be used together with the electrochem-

ical potential for monitoring the etching dynamics.

### B. Microscopic description of the etching process

Under normal conditions of temperature, the layer in contact with the liquid is passivated spontaneously thus isolating the metallic sample from the etchant action. When the focused laser spot heats a small area on the surface the passivation layer is removed and the thermally-activated chemical etching occurs there. The protons of the phosphoric acid (H<sub>3</sub>PO<sub>4</sub>) react with the iron, nickel and chromium of the steel producing hydrogen and dissolution of metal ions. The basic reactions can be described as :



with similar reactions for the ionization of the nickel and chromium. The etching reaction is exothermic in nature.

When the etching reaction dissolves the metal and consumes the etchant, a thin layer of solution in contact with the metallic surface develops a concentration gradient ranging from zero on the surface to the value of the bulk concentration. This is called the *Nernst diffusion layer* (NDL) and within its thickness  $\delta$ , the transport of ions of etchant and products of the reactions occurs exclusively by diffusion, limiting the etching reaction [10]. Outside this layer, convective transport maintains the concentration uniform at the bulk concentration. The value of  $\delta$  depends on the hydrodynamic conditions imposed by the etchant jet.

The NDL is not directly modelled in this work. We assume that its thickness  $\delta$  is almost negligible compared with the dimensions of the simulated topographies. It is worthy to note that the role of the Nernst diffusion layer is indeed essential in the real etching process. Variations of the dynamics of the jet due to its interaction with the surface can affect the value of the thickness  $\delta$  and in consequence, the transport of ions and reaction products. For example, if in a trough of a ripple the turbulence of the etchant flow allows a growing thickness  $\delta$ , this would imply a strong inhibition of the etching rate after certain depth threshold.

In experiments of wet-chemical etching of ceramics (without etchant jet), Lu *et al.* have found that the diffusive transport in the NDL is the main limiting factor of the etching rate [11]. Following their analysis and assuming that the etching rate decreases exponentially with the depth, an expression for the dependency of the etched depth with the feed velocity has been found to be in good agreement with experimental data for the LJE experiment using 5M H<sub>3</sub>PO<sub>4</sub> (see figure 4 in [5]). The function of the etchant jet is to enhance the etching rates reducing the NDL thickness  $\delta$ , to provide fresh etchant

and to remove dissolved material and reaction products. In addition, the jet creates a cooling effect that maintains the heating effect of the laser spot concentrated in a small region. Therefore the de-passivated zone and the resulting etching are highly localized. When the etchant jet velocity is increased the etching reaction is favored due to more fresh etchant but on the other hand it is inhibited due to the cooling effect. After the laser-jet leaves a region the surface is repassivated due to the decrease of the temperature and its topography will remain unaltered.

### III. OBTAINED KERFS AND INTRINSIC RIPPLE FORMATION

The etching front in most of the cases is stationary and the obtained kerf has, apart from small fluctuations, defined shape with almost constant width and depth. The bottom and walls of the kerfs are rough due to the stochastic character of the etching reactions. On the other hand, for certain sets of parameters of feed velocity, laser beam power or etchant jet velocity, oscillations of the etching front producing periodic ripples have been reported [5]. Here we will analyze the series of experiments with increasing power shown in figure 2.

There are two external sources which produce periodic structures that can be detected in the measurements for stationary etching fronts. First, due to its operation principle, the peristaltic pump introduces vibrations in the etchant jet in the range of 1-3Hz that can be detected in the power spectra of the electrochemical potential time series corresponding to periodic surface structures smaller than  $10\mu\text{m}$ . On the other hand, the  $xy$ -stage has an internal mechanism which controls its position each  $40\mu\text{m}$  resulting in small oscillations in the feed velocity  $v_f$  around a mean value. Nevertheless, the frequencies corresponding to the examined ripples are incommensurable with the frequencies of both the etchant pump and the controlling mechanism of the  $xy$ -stage. In consequence these can be discarded as external triggers of the obtained ripples.

From the point of view of the theory of pattern formation in continuous media, the appearance of ripples originated from instabilities is not unexpected because the etching front is formed in a system far from equilibrium due to the continuous and combined action of the laser beam and the jet of etchant. In general, one class of mechanisms for such instabilities arises from the existence of constraints and conservation laws in the system [12]. In the case of water jet cutting at high feed rates intrinsically generated ripples and striation patterns of the order of the water-jet diameter are formed at the side walls of the cut (see [13]). This fact has been used there as a criterion for distinguish between ripples triggered externally from the intrinsic ones.

The effective diameter of the etching front is not always constant for the LJE experiment. Certainly, more

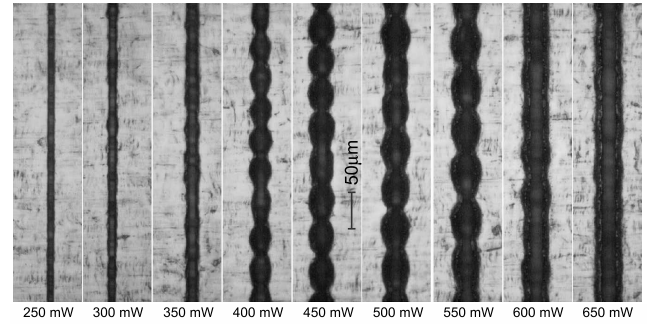


FIG. 2: Reproduced from Rabbow [5]. Optical microscope images showing a series of kerfs structured with increasing powers from 250mW to 650mW (etchant 5M  $\text{H}_3\text{PO}_4$ , feed velocity  $6\mu\text{m/s}$ , etchant jet velocity  $190\text{ cm/s}$ ). The kerfs for 250, 300 and 350mW are the result of an quasi-stationary etching front which widens with power. For powers greater than 350mW an instability in the etching front comes in and the obtained ripples seem to be product of a thermal runaway. An hypothesis on the intrinsic character of the ripples and some remarks on the mechanism which is creating this pulsating etching front are discussed in the text.

delivered power means higher temperatures and both the heated zone and the etching front become broader. For laser powers 250, 300 and 350mW an approximately stationary etching front produces kerfs with increasing width (see first three kerfs in the figure 2).

For powers larger than 350mW an instability appears producing ripples with increasing length and width. The ripples look like a product of thermal runaways which reach much broader areas than in the stationary etching front case. Each thermal runaway seems to appear above a temperature threshold, producing a quick broadening of the etching front. The broadening stops when the accelerated consumption of etchant inhibits further etching rates and the etching front shrinks until the conditions for the onset of the next thermal runaway are fulfilled. Note that during the ripple formation the absorption of laser radiation is also changing according to variations of the slope of the etching front. Probably this has a reinforcing effect on the pulsating etching front.

Based on these facts we formulate the hypothesis that above a power threshold, the instability creates a ripple with dimensions which are larger but proportional to the size of the stationary etching front that would appear if the mechanism that causes the instability would not act. This could explain why the ripple length increases with the power. For powers larger than 600W the ripples seem to overlap as the kerfs become deeper.

### IV. THE DISCRETE MODEL

Instead of trying a microscopical model with the interaction of all possible chemical and physical processes,

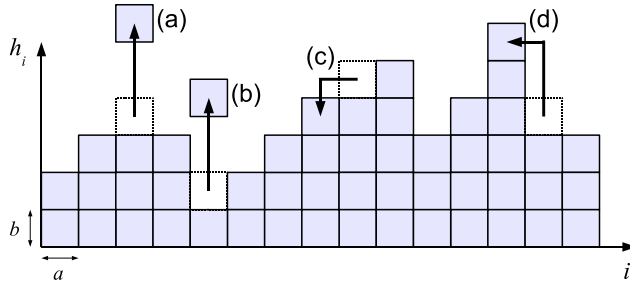


FIG. 3: Diagram representing the surface and the erosive and diffusive actions. (a) and (b) : sites submitted to the erosion rule. The probability of the being eroded is larger for the “valley” in (b) than for the “peak” in (a) according with an estimation of the curvature described in the section IV A 1. (c) and (d) Diffusive movements. The probability of the diffusion in (c) is close to one while for (d) it is very small according with a mechanism for creating a positive surface tension described in section IV A 2.

we formulate a minimal phenomenological description of the etching process based on some ideas of the theory of far from equilibrium evolving surfaces. A number of discrete growth models and continuum stochastic equations have been proposed to describe the kinetic roughening properties of surface growth and erosion [14]. For simulating the structures produced by the LJE technique, we have extended and adapted a stochastic 1D discrete solid-on-solid (SOS) model proposed by Cuerno and collaborators for the evolution of ion sputtered surfaces [9]. Within that framework they explain two stages: an early time regime characterized by ripples and late time regime where the roughening shows self-affine scaling behavior. It has been shown that this model is related with a noisy version of the Kuramoto-Sivashinsky equation which has been used extensively in the theory of unstable pattern formation [15].

A remarkable feature in experiments of ion sputtering is the presence of nearly periodic ripples, aligned parallel or perpendicular to the bombarding ion beam. [6],[16]. Relating the energy of the ion beam with sputtering yield, Bradley and Harper (BH) [17], found that the dependency of the erosion rate with the local surface curvature induces an instability, which is responsible for the formation of periodic ripples with a characteristic length. Troughs are eroded faster than peaks and this effect can be considered as a “negative surface tension” which competes with the smoothing mechanism of thermally activated surface diffusion (which is a positive surface tension).

The extended model is based on similar mechanism and the justification for applying it to ripples found in LJE is based on experimental evidence which shows that troughs are preferentially etched as compared to peaks. This can be explained as consequence of differences in the absorption of laser energy and the resulting heat pro-

cesses. Firstly, when the laser beam is acting on a trough, due to the geometry the reflected rays converge to the zone above the trough and eventually can produce multiple reflections inside. This means that the trough and its neighborhood can effectively absorb more laser radiation, more heat is produced, and in consequence the etching rate is enhanced. In the case of peaks reflected rays are dispersed in all directions and there are not secondary reflections. On the other hand, considering the cooling effect of the etchant jet due to heat convection, it is easy to imagine that peaks are cooled more efficiently than troughs where eddies and even stagnation of the fluid are more probable to appear. Then, the preferential heating and etching within troughs result in further increase of the local curvature, which in turn enhances the secondary reflections and heating due to poorer heat convective transport of heat by the etchant flow.

### A. The extension of the Cuerno model

The material to be eroded is represented in 1+1D by a lattice composed of cells of width  $a$  and height  $b$ , and the surface is represented by the integer valued height  $h_i$  where  $i = 1, \dots, L$  (see figure 3). The system size  $L$  is the number of cells in the horizontal direction and periodic boundary conditions apply for the height  $h_i$ . For each column, all the sites below the surface are occupied with cells, whereas all the sites above are empty. Overhangs are not allowed in this kind of models for simplifying both the simulation and the analytical approach.

The temporal evolution of this virtual surface takes into account rules for representing the erosion and the surface diffusion processes. In this kind of kinetic Monte Carlo simulations each erosion or diffusion event appears with a rate which has to be guessed through the use of all the available experimental and theoretical information [18]. The program defines a flat surface (one of the possible initial conditions), selects a site and invokes with probability  $f$  the erosion rule and with probability  $1 - f$  the diffusion rule. The process of selection of sites or rules to be applied is performed using a random number generator described in [19].

#### 1. The extended erosion rule

The erosion probability  $p_e$  for a cell at the site  $i$  is estimated as the product  $p_e = p_\kappa Y_i$ . The quantity  $p_\kappa$  corresponds to the probability of being eroded depending on the curvature of the surface at the site and accounts for the unstable erosion mechanism that exists in the physical system. The value of  $p_\kappa$  is larger for positive curvatures than for negative ones (see Figure 3 (a) and (b)). In the Cuerno model for ion sputtering the dependency of the erosion rate on the angle of incidence  $\varphi$  between the beam and a tilted portion of the surface is

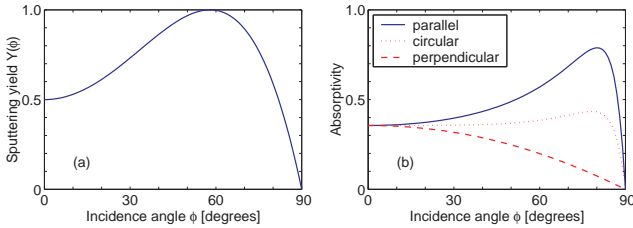


FIG. 4: (a) The sputtering yield dependence with the angle of incidence. The function used in the simulations is  $Y(\varphi) = 0.5 + 0.979\varphi^2 - 0.479\varphi^4$  and  $Y(0^\circ) = 0, Y(57.3^\circ) = 1, Y(90^\circ) = 0$ . (b) Absorptivity of polarized light versus incidence angle for a flat iron surface (based on [20]). Plane of polarization parallel to the incidence plane (continuous line), circular polarization (dotted line), plane of polarization parallel to the incidence plane (dashed line). The coefficient of refraction is  $n = 3.81$  and the attenuation coefficient is  $k = 4.44$ .

described by the sputtering yield function (from [15]):

$$Y_i = Y(\varphi_i) = y_0 + y_1\varphi_i^2 + y_2\varphi_i^4 \quad (3)$$

where  $\varphi_i$  is the incidence angle formed by the incoming beam and the normal direction defined on the surface at the site  $i$ . We will use the same function for the LJE case based of the fact that absorption of polarized light by flat metallic surfaces has similar functional dependence (in the case of electric field parallel to the plane of incidence or even circular polarization, see figure 4). The nonlinearity introduced by this yield (absorption) function becomes relevant at late regimes when large slopes develop, then the ripples will be strongly distorted and the surface will have a rough morphology.

We propose to replace the “box rule” by a direct estimation of derivatives, the angles and the curvatures based on a finite central differences method around a selected site. The first derivative or gradient of the surface at a point  $i$  is  $\nabla_i = (h_{i-1} - h_{i+1})/2a$  and the angle  $\varphi_i$  that the surface form at this site is estimated by  $\varphi_i = \arctan \nabla_i$ . This angle corresponds to the incidence angle used in the formula (3). The second derivative is  $\nabla_i^2 = (h_{i-1} - 2h_i + h_{i+1})/a^2$ . The curvature can be estimated using the standard formula  $\kappa_i = \nabla_i^2(1 + (\nabla_i)^2)^{-3/2}$ .

Due to the discreteness of the height  $h_i$  the values obtained with this formulae varies drastically from one site to the other. To attenuate this problem, the values for the angles and curvatures are computed not only for the site  $i$  but also for its neighbors  $i - 1$  and  $i + 1$ . Then the mean value of the angle for the site  $i$  is  $\overline{\varphi_i} = (\varphi_{i-1} + \varphi_i + \varphi_{i+1})/3$  and the mean curvature is  $\overline{\kappa_i} = (\kappa_{i-1} + \kappa_i + \kappa_{i+1})/3$ . This procedure takes into account the values of five sites  $(h_{i-2}, h_{i-1}, h_i, h_{i+1}, h_{i+2})$  and provides a smoothed estimation of the angles and curvatures which will influence strongly the evolution of the topography of the surface.

Taking into account these modifications in the algorithm, it is necessary to introduce two new parameters for estimating the curvature dependent erosion probability  $p_\kappa$ . First, the maximum of the possible positive curvature  $\kappa_{max}$  (the minimum  $\kappa_{min}$  is the negative of this value). Second, the minimum of the curvature dependent erosion probability  $p_{\kappa,min}$ . The obtained values of the curvature  $\kappa_i$  are mapped by a linear transformation in such a way that for  $\kappa_i = \kappa_{max}$  the curvature dependent erosion probability is  $p_\kappa = p_{\kappa,max} \equiv 1$  and when  $\kappa_i = \kappa_{min}$  then  $p_\kappa = p_{\kappa,min}$ . In the case that the computed curvature  $\kappa_i$  were larger than  $\kappa_{max}$  the algorithm assigns  $\kappa_i = \kappa_{max}$ . Similarly when  $\kappa_i < \kappa_{min}$  then  $\kappa_i = \kappa_{min}$ .

## 2. The diffusion rule

This rule is implemented in the same way proposed in the original Cuerno model. The probability of a diffusive movement of a selected cell  $i$  is evaluated selecting at random one of the two nearest neighbors and computing the hopping probability (see [21])

$$w_i^\pm = \frac{1}{1 + \exp(\Delta\mathcal{H}_{i \rightarrow i \pm 1}/(k_B T))} \quad (4)$$

here  $\Delta\mathcal{H}_{i \rightarrow i \pm 1}$  is the energy difference between the final and initial states of the move,  $k_B$  is the Boltzmann constant and  $T$  is the temperature. This surface energy is defined through the Hamiltonian :

$$\mathcal{H} = \frac{J}{b^2} \sum_{i=1}^L (h_i - h_{i+1})^2 \quad (5)$$

where  $J$  is a coupling constant through which the nearest neighbor sites interact and  $b$  is the height of the cells. Diffusion movements which produce final states with lower surface energy are then highly preferred (see figure 3(c) and (d)).

## B. Scaling of the extended Cuerno model

As usual in the field of far from equilibrium interfaces, we are interested in the temporal behavior of the surface width defined as :

$$W(t) = \sqrt{\frac{1}{L} \sum_{i=1}^L (h_i(t) - \langle h(t) \rangle)^2} \quad (6)$$

where  $L$  is the system size and  $\langle h(t) \rangle$  is the mean value of the all heights of the surface at the time  $t$ . The width  $W(t)$  can be considered as a characterization of the roughness and it is evaluated averaging over a number of different realizations of the random number seed. In order to evaluate an eventual scaling behavior  $W(t) \sim t^\beta$

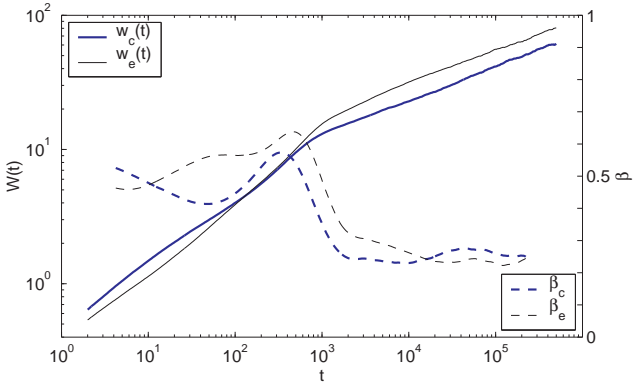


FIG. 5: Comparison of the scaling of the surface width for the Cuerno and the extended model. For the Cuerno model : The surface width  $W_c(t)$  (bold continuous line) and the corresponding growth exponent  $\beta_c$  (bold dashed line). Parameters:  $L = 2048$ ,  $f = 0.5$ ,  $J/(k_B T) = 5$ . For the extended model : The width  $W_e(t)$  (thin continuous line) and corresponding growth exponent  $\beta_e$  (thin dashed line). The extra parameters of the extended model are the closest possible to the Cuerno model :  $a = 1$ ,  $p_{c,min} = 1/7$ ,  $\kappa_{max} = 2$ .

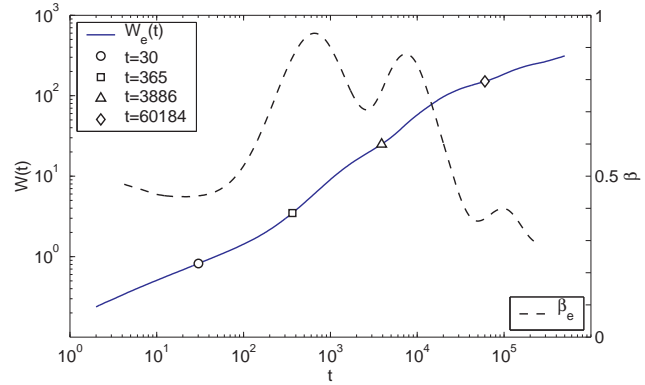


FIG. 6: Temporal evolution of the surface width  $W_e(t)$  (continuous line) and growth exponent  $\beta_e$  (dashed line) of the extended model for the parameter set used in the section V. The surface's morphology at times corresponding to  $t = 30$  (○ symbol),  $t = 365$  (□ symbol),  $t = 3886$  (△ symbol) and  $t = 60184$  (◊ symbol) is analyzed in the figure 7. Extended model parameters :  $L = 2048$ ,  $f = 0.1$ ,  $J/(k_B T) = 5$ ,  $a = 2$ ,  $p_{\kappa,min} = 0.15$ ,  $\kappa_{max} = 0.0825$ .

within an interval, the growth exponent  $\beta$  is estimated by the method of the consecutive slopes (see [14], page 305). For all the forthcoming figures and analyzes, the time unit is chosen to correspond to  $L$  erosion or diffusion rule invocations.

In order to verify the connection of the extended model with the original Cuerno model, the evolution of the width surface for both is compared in the figure 5. The system size is  $L = 2048$  and the width values were averaged over 100 different realizations. The probability of invoking the erosion rule is  $f = 0.5$  (the diffusion rule is invoked with probability  $1 - f = 0.5$ ) and the constant associated with the diffusion is  $J/(k_B T) = 5$ . The extra parameters of the extended model ( $a = 1$ ,  $p_{\kappa,min} = 1/7$ ,  $\kappa_{max} = 2$ ) have been chosen to reproduce as closely as possible the box rule for the erosion probability of the Cuerno model. For both cases the same ‘yield’ function is used  $Y(\phi) = 0.5 - 0.479\phi^2 + 0.979\phi^4$ .

The scaling properties are similar, showing first a rough interface at early times, then a strong increase of the growth exponent  $\beta$  due to the onset on the instability which create ripples, and finally a drop due to the stabilizing and roughening effect of the non-linear terms. However, the scaling behavior is not identical. A precise identification of the limits of the ripple regimes is difficult because they depend on each realization and the criterion to distinguish between fluctuations and proper ripples. The ripple regime for the Cuerno model can be estimated to be  $t \sim \{300, 1000\}$  while for the extended case the onset of the instability occurs earlier and the ripple regime lasts longer. The ripples in the extended model are larger in amplitude and present a quasi-sinusoidal shape.

The application of the extended model for the simu-

lation of the LJE that is presented in the next section requires to exploit the flexibility of the new parameters in order to generate ripples of similar size of the laser beam. In addition, the ripples should be clearly distinguishable from the inherent fluctuations and roughness produced by the stochastic character of the model. Accordingly, the scaling properties and the morphology evolution for a different parameter set will be analyzed in the rest of this section. The probability of invoking the erosion rule is  $f = 0.1$  (the diffusion rule is invoked with probability  $1 - f = 0.9$ ) and the constant associated with the diffusion is  $J/(k_B T) = 5$ . For weighting the curvature’s erosion probability  $p_{\kappa}$  the values  $a = 2$ ,  $p_{\kappa,min} = 0.15$ ,  $\kappa_{max} = 0.0825$  have been used. The system size is  $L = 2048$  and the width values were averaged over 100 different realizations.

The figure 6 shows the temporal evolution of the width  $W_e(t)$  and its growth exponent  $\beta_e$  for this parameter set. The ripple regime is much longer than in the cases presented in figure 5 and the obtained ripples have a larger amplitude. For times  $t \lesssim 100$  the exponent  $\beta$  is lower than the value 0.5 characteristic of random erosion. After  $t \gtrsim 100$  a strong increase of the value of  $\beta$  which is associated with the onset of the ripple regime. During the interval  $700 \lesssim t \lesssim 8 \times 10^3$  there is an oscillation of  $\beta$  but its values remain relatively high. The origin and meaning of this oscillation is currently unknown. For  $8 \times 10^3 \lesssim t \lesssim 4 \times 10^4$  a sudden decay of the growth exponent appears and for  $t \gtrsim 4 \times 10^4$  the  $\beta$  value fluctuates below 0.4.

The figure 7 shows a portion of the surface for the four times which are indicated with symbols in the figure 6. The left column shows the height  $h_i^*$  which is the height minus its average value at each time  $h_i^* = h_i - \langle h_i \rangle$ . The

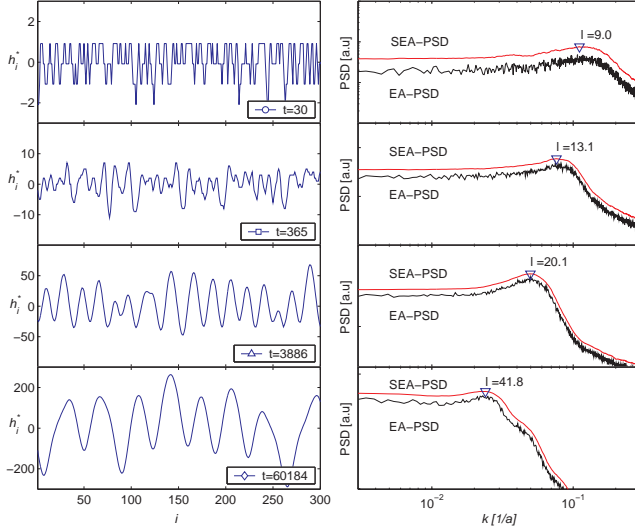


FIG. 7: Four different stages of the evolution of the surface for the extended Cuerno model corresponding to the times referred in figure 6. The left column shows the height  $h_i^*$  (note that all vertical scales are different). The real system size is  $L = 2048$  but only 300 points are shown in order to appreciate details of the morphology of the surface. The right column shows the corresponding *ensemble average* of the power spectral density EA-PSD (lower curve) and the *smoothed ensemble average* of the power spectral density SEA-PSD (upper curve, shifted in the vertical direction for clarity of presentation). The local maxima of the SEA-PSD (indicated by the  $(\nabla)$  symbols) is used to estimate the mean value of the ripple length  $l$  of each stage.

right column shows the corresponding to the *ensemble average* of the power spectral density EA-PSD computed with 100 realizations and  $L = 2048$ . The PSD is represented in a logarithmic scale with arbitrary units and the horizontal axis corresponds to the wavelength number  $k$ . A moving window average over 10 points is applied on the spectra and the resulting *smoothed ensemble average* of the power spectral density SEA-PSD appears above the EA-PSD curve. The local maxima of the SEA-PSD (indicated by the  $(\nabla)$  symbols) can be used to estimate the mean value of the ripple length  $l$  of each stage.

In the rough surface corresponding to  $t = 20$  ( $\circ$  symbol) the integer values of the heights are noticeable. For the time  $t = 365$  ( $\square$  symbol) the ripples start to appear but their shape and length are highly irregular. More soft and larger ripples are found for times in the regime around to  $t = 3886$  ( $\triangle$  symbol) and the length estimated by the SEA-PSD method is approximately  $l = 20.1a$ . It is observed that the ripple length is increasing with time due to the merging of ripples : small ripples are assimilated by contiguous larger ripples which in turn develop a sinusoidal shape. For times  $t \gtrsim 4 \times 10^4$  the non-linearity introduced by the sputtering yield  $Y_i$  starts to show its effect on the morphology of the surface : ripple coarsening and strong modulation of the surface

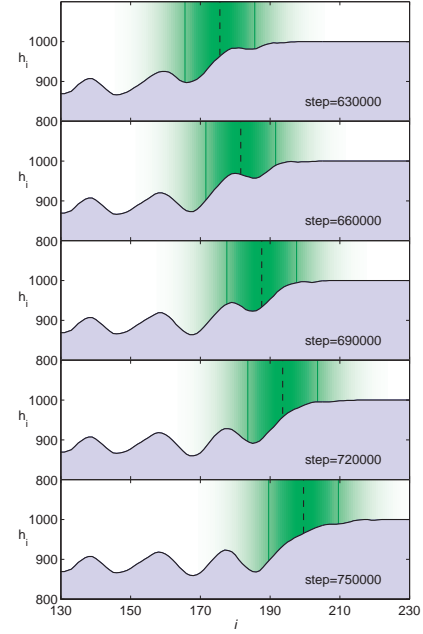


FIG. 8: Five stages of the formation of a single ripple. The center of the moving gaussian beam is represented by the vertical dashed line. The vertical continuous lines correspond to one standard deviation ( $-\sigma$  at left and  $+\sigma$  at right in a reference system located on the beam). The radius of the beam is  $r = 10a$  and corresponds to  $\sigma$ . The feed velocity is  $0.004a$  per step. The erosion/diffusion invocation probability is  $f = 0.1$  and for weighting the erosion probability the values  $a = 2$ ,  $p_{\kappa, \min} = 0.15$ ,  $c_{\max} = 0.0825$  have been used.

by small wave-numbers (or large lengths).

The increasing ripple length is a deviation from linear analysis predictions on the Kuramoto-Sivashinsky description. It is originated from non-linear terms that can be examined in the derivation of the continuum equation for this discrete model as it is shown in [22]. Analogous phenomena have been reported for experiments on ion sputtering [23],[24] and laser ablation [25] among others.

## V. THE SIMULATION OF KERFS FORMATION IN LJE

In order to simulate the action of laser beam, the selection of the site to be submitted to erosion or diffusion rules is randomly generated within a moving gaussian probability distribution

$$G(x, t) = \frac{1}{\sigma\sqrt{2\pi}} e^{-(x-v_f t)^2/(2\sigma^2)} \quad (7)$$

where  $\sigma$  corresponds to one standard deviation and  $v_f$  is the feed velocity. In the simulation the surface is considered fixed while the laser beam moves. The effective radius of the beam is defined to be equal to  $\sigma$ . For a fixed

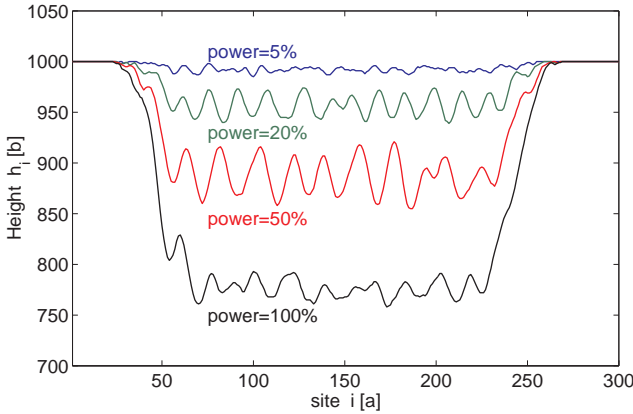


FIG. 9: Profile of the kerfs for powers of 5%, 20%, 50% and 100%. The horizontal axis is the site number  $i$  is measured in units of  $a$  (width of the cell) and its corresponding height is measured in units of  $b$  (height of the cell). The used laser beam radius is  $10a$ , the number of steps  $10^6$  and the feed velocity is  $0.002a$  per step. The erosion/diffusion invocation probability is  $f = 0.1$  and for weighting the erosion probability the values  $a = 2$ ,  $p_{\kappa, \min} = 0.15$ ,  $c_{\max} = 0.0825$  have been used.

region on the surface the action of the moving laser consists in the combined action of erosion and diffusive rules during a characteristic time  $2\sigma/v_f$ . Depending upon  $v_f$  the resultant moving etching front will eventually develop instabilities which in turn will give rise to ripple structures. After the beam leaves the region the surface has acquired a topography that depending on the velocity, power, radius of the beam and other parameter corresponds roughly to one of the stages analyzed in the figure 6. It is worthy to note that most of the time the model's rules are acting on the tilted surface of the etching front and due to the slope dependency of the erosion probability, the final topographies will depend in a complex way on all the parameters of the model.

Figure 8 shows the process of creation of a single ripple for a feed velocity of  $0.004a$  per step and a beam radius  $r = 10a$  (the model parameters are the same used in the Figures 6 and 7 of the previous section). Typically, a valley is created at the forefront of the beam from a small but growing depression on the surface (there is one at the right of the center of the laser beam for the frame corresponding to step=63000). When the center of the laser beam passes through a valley, the rate of erosion increases, and the valley grows as long as the rearmost part of laser beam is acting. The peaks alternating the valleys are eroded at a lower rate due to their negative curvature. In summary, for this parameter set the local and temporal action of the laser works as an amplifier of small instabilities on the surface.

It is possible to simulate different laser powers within the model, introducing an additional weight to the probability of applying the erosion and diffusion rules. Increasing the power the bottom of the obtained kerf de-

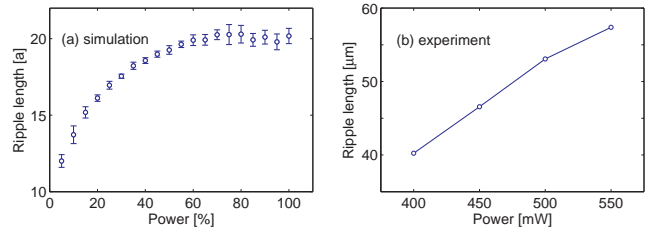


FIG. 10: (a) Simulation : Ripple length of the bottom's kerfs for different powers corresponding to the parameters used in the figure 9. An ensemble of 10 realizations of 16384 points long bottom of the kerf has been used to estimate a mean value for the ripple length and its uncertainty (see details in the text). (b) Experiment: Ripple length for the power values 400, 450, 500, 550 mW corresponding to the kerfs shown in 2.

velops topographies corresponding to later stages of the evolution of width shown in figure 6. For power=5% the kerf is shallow and rough, while for powers corresponding to 20% and 50% regular ripples are obtained. For this set of parameters and for powers larger than 60%, the non-linear effects stemming from the nonlinear yield function take over diminishing the widths and suppressing the regularity of the ripples. Summarizing, a ripple regime generated within an interval of powers ( $\sim 20$ -60% power) is found and can be compared with the ripple regime obtained in the experiment shown in figure 2.

The simulated ripples are not perfectly periodic and harmonic, therefore it is only possible to estimate the ripple length as the mean value of a band of wave-numbers in the power spectral density. To obtain an ensemble average, 10 realizations with 16384 points of the bottom of the kerf have been used. For each realization, the maximum of a smoothed version of the PSD (100 points moving window average) determines its corresponding ripple length. The uncertainty of the ripple length is estimated by means of the standard deviation over the 10 realizations. Figure 10(a) shows the ripple length dependency on the laser power. The ripple length increases up to a saturation value close to  $20a$ . For powers greater than 60% the non-linear regime starts and the ripples become irregular.

In the figure 10(b) the ripple length of the experimental series corresponding to the powers 400, 450, 500 and 550mW are shown in figure 2. Of course, four points are not enough to draw a conclusion about this dependency. We will explore further this correspondence when more experimental data become available.

## VI. CONCLUSIONS

The extended discrete model applied to the simulation of formation of kerfs reproduces qualitatively some of the main characteristics of microstructures produced

by the LJE experiment. The basic mechanism based on competition of curvature dependent erosion and surface diffusion produces a ripple regime which appears between roughening at earlier and later stages of the surface evolution. Compared with the original Cuerno model the extended model produces a longer time interval where ripples occur which is more appropriate for the simulation of the moving etching source of the LJE experiment. This is accomplished applying the erosion and diffusion rules within a moving spatially gaussian probability distribution and, taking advantage of the probabilistic nature of the Monte Carlo method, it is possible to simulate the laser power distribution, laser beam spot size and feed velocity. In analogy with a series of experiments, variations of the laser power reveal a regime with an unstable etching front and in consequence, regular ripples in the bottom of the kerfs. In addition, the ripple length is growing with increasing power. Outside of this interval of power values, the kerfs present a rough morphology at the bottom.

This simple phenomenological model does not pretend to simulate the complex behavior of the process. Instead

it can be considered as a guide to propose experiments that reveal more relevant features of the ripple formation and the structuring process in general. The next step is to incorporate the temperature field and the dynamics of the concentration of etchant in the Nernst diffusion layer. This could allow us to understand the conditions for the onset of the thermal runaway responsible of ripple formation. For a better comparison with the experimental results a further obvious step is the generalization of the model to 2+1 dimensions.

### Acknowledgments

We gratefully acknowledge Simeon Metev and Andreas Stephen for the support at the BIAS Institute. We thank Rudolf Friedrich, Stefan Linz, Hans J. Herrmann, Rudolf Hilfer, Alexei Kouzmitchev, Bernd Lehle, Volker Schatz and Ferenc Kun for helpful discussions and suggestions. This work was funded by the Volkswagen-Stiftung grant I/77135.

---

[1] R. J. von Gutfeld and K. G. Sheppard. Electrochemical microfabrication by laser-enhanced photothermal processes. *IBM Journal of Research and Development*, 42(5):639–653, 1988.

[2] R. Nowak and S. Metev. Thermochemical laser etching of stainless steel and titanium in liquids. *Applied Physics A*, 63:133–138, 1996.

[3] Andreas Stephen, Thorsten Lilienkamp, Simeon Metev, and Gerd Sepold. Laser-assisted chemical micromachining of metals and alloys. *RIKEN Review : Focused on 2nd International Symposium on Laser Precision Microfabrication (LPM 2001)*, 43:56–62, january 2002.

[4] Simeon Metev, Andreas Stephen, Jörg Schwarz, and Carsten Wochnowski. Laser-induced chemical micro-treatment and synthesis of materials. *RIKEN Review: Focused on Laser Precision Microfabrication (LPM 2002)*, (50):47–52, january 2003.

[5] Thomas Rabbow and Peter Jörg Plath. Self-organized structure formation in organised microstructuring by laser-jet etching. (To be published). Institute für Angewandte und Physikalische Chemie-AG Chemische Synergetik. Universität Bremen.

[6] Maxim A. Makeev, Rodolfo Cuerno, and Albert -László Barabási. Morphology of ion-sputtered surfaces. *Nuclear Instruments and Methods in Physics Research B*, 197:185–227, 2002.

[7] U. Valbusa, C. Boragno, and F. Bautier de Mongeot. Nanostructuring surfaces by ion sputtering. *Journal of Physics : Condensed Matter*, 14:8153–8175, 2002.

[8] R. Friedrich, G. Radons, and A. Ditzinger, T. Henning. Ripple formation through and interface instability from moving growth and erosion sources. *Physical Review Letters*, 85(23):4884–4887, 2000.

[9] Rodolfo Cuerno, Hernán A. Makse, Silvina Tomasone, Stephen T. Harrington, and H. Eugene Stanley. Stochastic model for surface erosion via ion sputtering : Dynamical evolution from ripple morphology to rough morphology. *Physical Review Letters*, 75(24):4464–4467, 1995.

[10] Allen J. Bard and Larry R. Faulkner. *Electrochemical Methods. Fundamentals and Applications*. John Wiley & Sons, 1980.

[11] Yong Feng Lu, M. Takai, S. Nagatomo, and S. Namba. Wet-chemical etching of Mn-Zn ferrite by focused Ar+-laser irradiation in H<sub>3</sub>PO<sub>4</sub>. *Applied physics A*, 47:319–325, 1988.

[12] M. C. Cross and P. C. Hohenberg. Pattern formation outside of equilibrium. *Review of Modern Physics*, pages 851–1112, 1993.

[13] G. Radons, T. Ditzinger, R. Friedrich, A. Henning, A. Kouzmichev, and E. Westkämper. *Nonlinear dynamics and control of ripple formation in abrasive water-jet cutting*, chapter 22, pages 391–410. Wiley-VCH, 2004.

[14] Albert-László Barabási and H. Eugene Stanley. *Fractal Concepts in Surface Growth*. Cambridge University Press, 1995.

[15] Kent Baekgaard Lauritsen, Rodolfo Cuerno, and Hernán A. Makse. Noisy Kuramoto-Sivashinsky equation for an erosion model. *Physical Review E*, 54(4):3577, 1996.

[16] S. Facsko, T. Dekorsy, C. Koerdt, C. Trappe, A. Kurz, H. Vogt, and H.L. Hartnagel. Formation of ordered nanoscale semiconductor dots by ion sputtering. *Science*, 285:1551–1553, 1999.

[17] Mark Bradley and James Harper. Theory of ripple topography induced by ion bombardment. *Journal of Vacuum Science and Technology*, 6(4):2390–2395, 1988.

[18] Peter Kratzer and Matthias Scheffler. Surface knowledge: toward a predictive theory of materials. *Computing in Science and Engineering*, 3(6):16–25, 2001.

[19] William H. Press, Saul A. Teukolsky, William T. Vet-

terling, and Brian P. Flannery. *Numerical Recipes in FORTRAN, the Art of Scientific Computing*. Cambridge University Press, 1992.

[20] Lawrence Yao. Laser machining processes. section 2.9: Reflection and absorption of laser beams, 2000. <http://www.columbia.edu/cu/mechanical/mrl/ntm/level2/ch02/html/l2c02s09.html>.

[21] Martin Siegert and Michael Plischke. Solid-on-solid models of molecular-beam epitaxy. *Physical Review E*, 50:917–931, 1994.

[22] Alejandro Mora and Maria Haase. A first stochastic model for ripple formation in laser-induced etching. part II: Derivation of the continuum equation. *To be published*.

[23] S. Habenicht, J. Lieb, K.P. Koch, and A.D. Wieck. Ripple propagation and velocity dispersion on ion-beam-eroded silicon surfaces. *Physical Review B*, 65:115327, 2002.

[24] S. Rusponi, G. Costantini, C. Boragno, and U. Valbusa. Scaling laws of the ripple morphology on Cu(110). *Physical Review Letters*, 81, 1998.

[25] Ionut Georgescu and Michael Bestehorn. Pattern formation upon femtosecond laser ablation of transparent dielectrics. arXiv:cond-mat/0411244 v1 10 Nov 2004.